The hydrodynamics of drop impact onto chemically structured surfaces

2005 J. Phys.: Condens. Matter 17 S607

(http://iopscience.iop.org/0953-8984/17/9/019)

INSTITUTE OF PHYSICS PUBLISHING JOURNAL OF PHYSICS: CONDENSED MATTER

J. Phys.: Condens. Matter **17** (2005) S607–S622 doi:10.1088/0953-8984/17/9/019

The hydrodynamics of drop impact onto chemically structured surfaces

T Michel[1], U Mock[2], I V Roisman[1,3], J Rühe[2] and C Tropea[1]

[1] Chair of Fluid Mechanics and Aerodynamics, Technical University Darmstadt, Darmstadt, Germany
[2] Chemistry and Physics of Interfaces, Institute for Microsystem Technology, University of Freiburg, Freiburg, Germany
[3] Faculty of Mechanical Engineering, Technion–IIT, Haifa, Israel

Received 24 November 2004, in final form 29 November 2004
Published 18 February 2005
Online at stacks.iop.org/JPhysCM/17/S607

Abstract

The normal and inclined impact of liquid drops onto chemically structured surfaces has been studied experimentally and theoretically. The surface functionalization comprised a self-assembly process of a covalently bound monochlorosilane on a silicon substrate, followed by a photochemical attachment of a polymer of defined hydrophilicity and a subsequent deep UV ablation step to create a local spot of high wettability in a region of low wettability so that a self-centring effect of the impacting liquid could be achieved.

Experimentally the impact is observed using a high-speed camera, changing the impact velocity, the impact displacement from the wettable spot and the inclination of the surface. The temporal spread of the drop was recorded, yielding also the macroscopic dynamic contact angle as a function of time. A theoretical model of the drop impact is developed, based on a mass balance and on a momentum balance which includes capillary forces and viscous drag, and which accounts for the inertial and wettability effects. The theoretical predictions for the time evolution of the drop edges agree well with the experimental data.

1. Introduction

Drop impact onto a wall is one of the key phenomena involved in many industrial processes such as spray cooling, spray coating, fuel injection and ink jet printing. The drop impact problem has been studied for well over a century [1, 2], and today many features of the process—drop deformation, spreading, receding and splash—are known. The main parameters of drop impact are the initial drop diameter D_0, impact velocity U_0, density ρ of the liquid, viscosity μ, and surface tension σ. The usual dimensionless parameters used in the description of drop impact are the Reynolds number $Re = \rho U_0 D_0/\mu$ and the Weber number $We = \rho U_0^2 D_0/\sigma$. In the

case of drop impact onto a dry, partially wettable substrate the advancing and receding contact angles, Θ_{adv} and Θ_{rec}, govern the behaviour of the drop on the wall surface. In addition, the roughness of the substrate can influence the outcome of drop impact; in particular, roughness promotes splash phenomena at lower impact velocities. The properties of the surrounding gas usually do not enter the problem. Several outcomes of drop impact onto a dry wall, depending on the above mentioned parameters, have been identified: rebound, partial rebound, receding break-up, corona splash, prompt splash and deposition [3].

One necessary condition for high-quality drop deposition in printers, onto bio-chips [4], or for agricultural purposes [5], is a drop impact below the splash threshold, avoiding any break-up of the liquid drop. The initial deformation of the drop on the wall is followed by a spreading and in some cases a subsequent receding phase. Whether a receding phase occurs depends on the maximum spreading diameter achieved and on the receding contact angle, as outlined in [6]. Drop ejection from the surface can occur either directly through splashing during the initial spreading phase or after the receding phase, when a central jet may be ejected from the surface. The normalized diameter of the spreading drop is often referred to as the spread factor, and it has been experimentally investigated as a function of time for a large number of impact parameters and surfaces with uniform wetting properties [7–12]. Drop impact onto inclined surfaces has been less well documented [13]. Initial studies show that splash and rebound thresholds can be unified for various impact angles if the wall normal velocity is used in the Reynolds and Weber numbers.

One further method to control the outcome of drop impact and especially to influence the splash threshold is the use of additives in the liquids [14, 15]. Such effects have not been extensively studied and will not be considered in the present work.

Many experimental results have been successfully computed using finite-volume codes employing a volume-of-fluid approach to capture the free surface of the drop [16–19]. For inertial dominated impacts or spreading phases, the contact line treatment does not appear to be very critical; however, the correct prediction of a receding drop will depend very much on the contact line dynamics. Recent studies comparing measured and predicted dynamic contact angle for both the advancing and receding stage have shown that contact angle hysteresis must be taken into account to achieve good prediction [13].

In the present work, normal and inclined drop impacts onto structured substrates are experimentally studied. The structure of the silicon wafer substrate refers to the wettability, which is varied by a coating process. The surface functionalization comprised a self-assembly process of a covalently bound monochlorosilane on a silicon substrate, followed by a photochemical attachment of a polymer of defined hydrophilicity and a subsequent deep UV ablation step to create a local spot of high wettability in a region of low wettability so that a self-centring effect of the impacting liquid could be achieved. Upon irradiation the benzophenone group can react with almost any C–H-group containing polymer of defined hydrophilicity yielding ultra-thin layers in the nanometre range [20]. A subsequent ablation process through a mask leads to a defined pattern formation [21]. This surface functionalization enables surfaces with areas of different wettability to be fabricated. Surfaces with a circular area of high wettability embedded in a region of low wettability are used for the present impact experiments. A liquid which is situated at the borderline between both regions experiences a resulting force towards the hydrophilic spot. This produces a *self-centring* effect, which means that this force moves the liquid onto the hydrophilic spot.

In this study the impact velocity of the drop, the displacement between the impact point and the wettable spot, and the inclination angle of the surface were varied. The impact event was observed from the side, from which the temporal development of the 'front' and 'back' edge of the drop could be monitored, as well as the corresponding macroscopic contact angle. Using

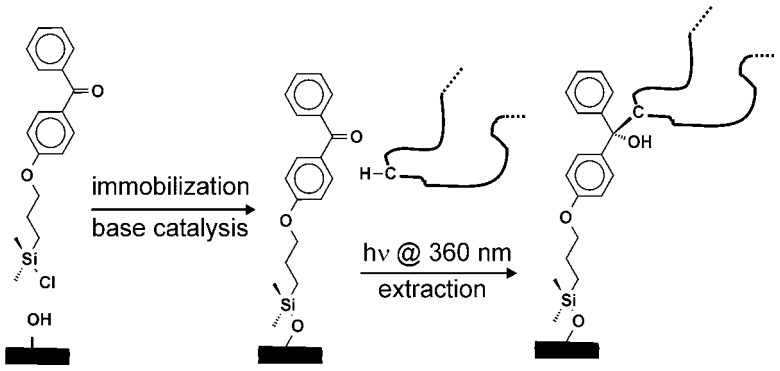

Figure 1. Schematic depiction of the surface functionalization using a photoactive benzophenone group bearing monochlorosilane.

appropriate time sampling, the local contact line velocity could also be estimated. Special attention was given to the conditions under which the entire liquid volume ended on the spot and to the behaviour of the dynamic contact angle. Thus, the parameters of drop impact under which the self-centring of the drop was achieved could be determined.

The drop impacting onto a rigid surface creates on it a thin radially expanding liquid film (lamella) bounded by a rim. This rim is formed by capillary forces and its motion is governed by the wettability effects, viscous drag, surface tension applied to the rim from the lamella, and inertia of the liquid entering the rim from the lamella. In [22] a theoretical model of drop impact onto a dry substrate of uniform contact angle was developed. In the present paper this model is generalized to take into account the local variations of the static contact angle on the surface of the substrate.

The experimental set-up, and a description of the process of the surface preparation and of the drop impact experiments are given in section 2. The hydrodynamics of drop impact is described in section 3 theoretically. A comparison of the experimental results and the theoretical predictions for the parameters of drop impact are presented and discussed in section 4. The conclusions are presented in section 5.

2. Experimental details

2.1. Surface preparation

Polystyrene surfaces with a defined wettability are obtained using a photochemical attachment of a polystyrene standard with a very low polydispersity ($M_n = 1400$ kg mol^{-1}, PD $= 1.05$, PSS) according to a procedure depicted in figure 1. In the first step a self-assembled monolayer of a photoreactive monochlorosilane is covalently linked to the silicon surface. Second, a dip-coated layer (dipping speed: 60 mm min^{-1}) of a 10 mg ml^{-1} solution of polystyrene in toluene (technical grade, Riedel-de-Haën, distilled over Na) is attached by UV-irradiation [16]. After Soxhlet-extraction in toluene for at least 15 h a polymer monolayer of 10 ± 2 nm thickness is obtained. A subsequent ablation step using a polymer contact mask leads to a decomposition of the polymer in the irradiated area [17]. The irradiated spot is etched for 30 s with a 1 M KOH solution in order to remove any remaining carbon particles.

The layer thicknesses were determined by ellipsometry ($\lambda = 632.8$ nm, $n = 1.59$, DRE-X 02 C, Dr. Riss GmbH) and a 1.6 kW x-ray reflectometer (Cu Kα, $\lambda = 0.154$ nm,

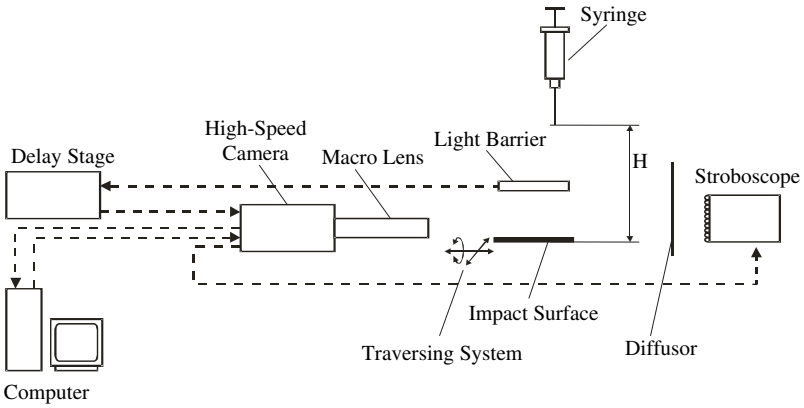

Figure 2. Schematic diagram of the experimental set-up.

Table 1. List of the substrates used in the experiments and their properties.

Substrate	Material	Contact angle	Spot
Surface I	Silicon wafer with a polystyrene coating	$\Theta_{adv} = 90°, \Theta_{rec} = 65°$	$\Theta_{spot} = 54°$
Surface II	Silicon wafer with a polystyrene coating	$\Theta_{adv} = 93°, \Theta_{rec} = 86°$	$\Theta_{spot} < 20°$

Bruker AXS D 5000). The layer roughness was measured using the AFM tapping mode at a resonance frequency of ∼360 Hz, using commercially available tips with a spring constant of ∼50 N m^{-1} (Nanoscope IIIa, Digital Instruments). On a 5 × 5 μm^2 area the rms roughness was determined to be 0.2 nm, which is comparable to the rms roughnesses obtained from x-ray reflectometry measurements (0.5 nm) and typical for polymer monolayers. Note that in terms of hydrodynamics this surface can be considered smooth, in no way influencing the splash behaviour of the impacting droplets. The ablation experiments were carried out using a Pen Ray lamp from L.O.T. Oriel, which has a significant output at low wavelength UV irradiation. Typical irradiation times were 12 h. Static contact angles were measured using a Dataphysics OCA20 set-up and Millipore water. The drop size was 2 μl in all cases. Table 1 provides the contact angles of the surfaces which were used for the experiments.

2.2. Experimental set-up

The experimental apparatus is pictured schematically in figure 2. Drops generated using a hypodermic syringe fall through a light barrier before impacting onto the surface mounted on a micrometre positioning table. The drop velocity is varied by varying the height of the syringe H and the velocity is estimated using the two image frames immediately before impact. The drop diameter is determined by the needle diameter: a 0.4 mm needle yields 2.5 mm drops whereas a 0.9 mm needle produces drops of 3.2 mm diameter.

Images are taken using a high-speed CMOS camera (Vosskühler HCC 1000(Strobe)) with 8 bit grey-scale resolution and frame rates of 922 fps (1024 × 512 pixels) or 1825 fps (1024 × 256 pixels). The light barrier, together with an adjustable delayer, provides the trigger to start the camera sequences of up to 2024 frames. Backlighting from an LED stroboscope with an illumination of 10 ms is triggered by the camera. A diffuser is used to achieve more

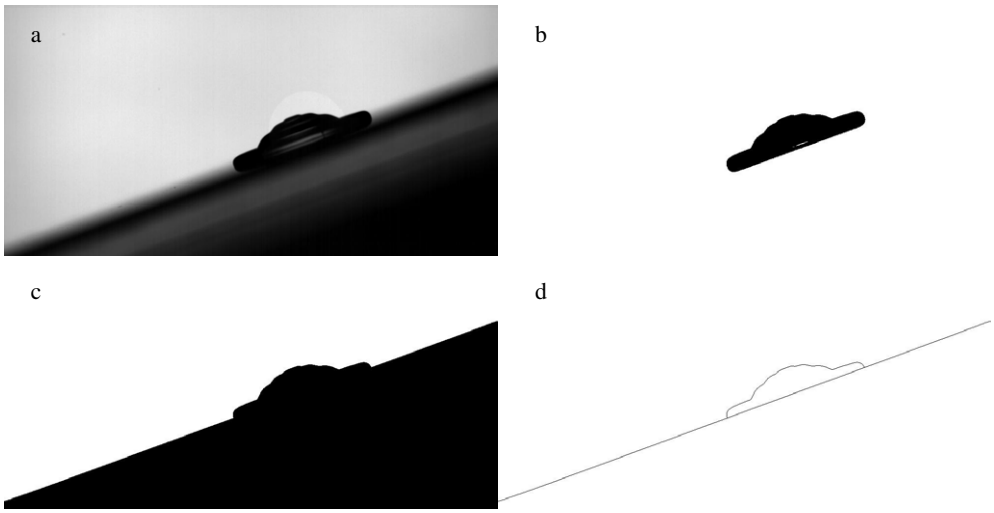

Figure 3. Detection of the drop contour. (a) Original image; (b) eliminated background; (c) replaced impact surface to eliminate mirror image; (d) drop and impact surface contour.

uniform illumination. All experiments were performed using distilled water ($\rho = 998\,\mathrm{kg\ m^{-3}}$; $\mu = 10^{-3}\,\mathrm{kg\ m^{-1}\ s^{-1}}$; $\sigma = 73 \times 10^{-3}\,\mathrm{N\ m^{-1}}$).

The present experiments were all performed using one camera capturing the side view of the droplet during impact, with a focal plane on the centreline of the hydrophilic spot. Further experiments using a second camera to acquire a top view are currently underway; these are especially interesting for capturing the asymmetric shape of the drop when traversing the hydrophilic spot or for inclined impacts. These results will be presented in a future publication. Nevertheless, the symmetry of the drop impact about the focal plane was very high, as was the repeatability.

2.3. Image processing

To correctly identify the drop surface contour a reference image is first acquired comprising the impact surface and a scaling needle of 0.91 mm diameter in the object plane. This reference image with extremely sharp and well defined contours is used to calibrate the edge grey value used to later detect the drop surface contour. The edge grey value (threshold) is chosen where the maximum value of the grey level derivative is found. The various steps in the image processing are exemplarily pictured in figure 3, starting with the original image of the drop at some time on an inclined surface, figure 3(a). The background is first eliminated by subtraction of those pixels with an equal grey value from an image before the drop enters the field of view. A threshold is then applied to sharpen the drop contour (figure 3(b)). This is the threshold determined using the reference image, as outlined above. The impact surface is added from the reference image as a black region to eliminate the mirror image of the drop on the surface (figure 3(c)). Finally the overall drop contour is identified. The drop and the known surface contour are shown in figure 3(d). From the sequence of contour data in time the following data are generated: initial drop diameter and velocity, impact time and position, contact line edge positions, wetted length on the impact surface, and drop apex height. The accuracy of the drop contour is one pixel. The contact angle is calculated from the original image using the gradient of the grey values obtained with a Sobel mask. The error in estimating the macroscopic contact angle is about 1° due to noise and about 3° quantization error.

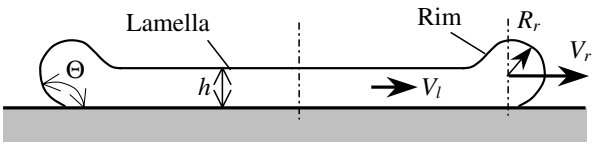

Figure 4. Sketch and nomenclature of the spreading drop.

3. Theoretical description of drop impact

The phenomenon of a single drop impact onto a dry wall can be subdivided into several main phases [6]. The first phase of duration $D_0/(U_0 t) < 1_{[\mathrm{tm1}]}$ is the *initial drop deformation*. During this phase the radially expanding thin film—the lamella—is formed on the surface. In the second phase the lamella continues to spread in the radial direction; however, the momentum in the lamella normal to the surface is negligibly small. At the end of the lamella a rim is formed due to the capillary forces. It moves with a velocity smaller than the velocity of the liquid in the lamella. The rim position determines the shape of the wetted spot on the substrate. This second phase, at times larger than $D_0/(U_0 t) = 1_{[\mathrm{tm2}]}$, will be called here *drop spreading*. However, if the substrate is hydrophobic, the rim will in fact also recede in this phase [6–10].

3.1. Initial drop deformation

During the initial phase of drop deformation its shape changes from an almost spherical shape to a disc-like shape. The momentum normal to the substrate (axial) is transformed into momentum parallel to the substrate, expanding radially in a thin lamella. The axial momentum is decreased by viscous forces present at the wall. In [22] creeping flow is assumed in this viscous layer. This assumption allows estimation of the pressure field in this layer, accounting also for capillary forces. The initial thickness h_{init} of the lamella is then estimated in [22] from the total mass and momentum balance of the drop during the first phase. It is found as the root of the following equation:

$$3We + 5(1 - \cos\Theta)Re\,\bar{h}_{\mathrm{init}} = 10\,Re\,We\,\bar{h}_{\mathrm{init}}^3 \tag{1}$$

where Θ is the average dynamic contact angle. Here and below the overbarred variables denote dimensionless parameters, with the initial drop diameter D_0 used as a length scale, and the impact velocity U_0 used as a velocity scale.

3.2. Drop spreading

The thickness of the lamella, h_{l}, reduces in time due to its radial spreading. Capillary forces acting at the edge of the lamella lead to the formation of a rim, whose radial velocity V_{r} is smaller than the velocity of the liquid in the lamella V_{l} (see figure 4). The motion of this rim determines the evolution of the spread factor in the spreading and receding phase.

The radial force per unit length of the rim includes the inertia of the liquid entering the rim from the lamella, $\rho h_{\mathrm{l}}(V_{\mathrm{l}} - V_{\mathrm{r}})^2$, the capillary force, $-\sigma$, the force associated with the wettability, $\sigma\cos\Theta$, and the viscous drag force, $-6\,\mu V_{\mathrm{r}}\sin\Theta/(1-\cos\Theta)$. This viscous drag force is estimated using the lubrication approximation.

The mass and the momentum balance equations of the rim yield the following ordinary differential equation for the dimensionless radial velocity of the rim:

$$\frac{\mathrm{d}\bar{V}_{\mathrm{r}}}{\mathrm{d}\bar{t}} = \frac{12\bar{R}_{\mathrm{r}}}{1 - 6\bar{R}_{\mathrm{r}}^2\bar{h}_{\mathrm{l}}}\left[\bar{h}_{\mathrm{l}}(\bar{V}_{\mathrm{l}} - \bar{V}_{\mathrm{r}})^2 - \frac{1-\cos\Theta}{We} - \frac{6\bar{V}_{\mathrm{r}}\sin\Theta}{Re(1-\cos\Theta)}\right], \qquad \text{for } \bar{r} = \bar{R}_{\mathrm{r}} \tag{2}$$

where $\bar{R}_r$ and $\bar{V}_r$ are the radius of the rim centreline and its velocity, and $\bar{h}_l$ and $\bar{V}_l$ are the thickness and the velocity of the lamella. The expressions for $\bar{h}_l$ and $\bar{V}_l$, satisfying the mass and the momentum balance in the lamella, are obtained in [23] in the form

$$\bar{h}_l = \frac{\bar{\eta}}{(\bar{t}+\bar{\tau})^2}, \qquad \bar{V}_l = \frac{\bar{r}}{(\bar{t}+\bar{\tau})^2} \tag{3}$$

with $\bar{\eta}$ and $\bar{\tau}$ being dimensionless constants. These parameters are estimated in [22] from the initial conditions as

$$\bar{\tau} = \frac{1}{\sqrt{12\bar{h}_{init}(1+12\bar{e}_S-12\bar{e}_D)}} - 1 \tag{4}$$

$$\bar{\eta} = h_{init}(1+\bar{\tau})^2 \tag{5}$$

where the terms $\bar{e}_S$ and $\bar{e}_D$ are the dimensionless surface energy and the dimensionless energy loss due to the viscous dissipation. These terms are defined as

$$\bar{e}_S = We^{-1}\left[1-\sqrt{\frac{2\bar{h}_{init}}{3}}-\frac{1-\cos\Theta}{6\bar{h}_{init}}\right] \tag{6}$$

$$\bar{e}_D = Re^{-1}\left(\frac{1}{20\bar{h}_{init}^3}+\frac{3}{5\bar{h}_{init}}\right). \tag{7}$$

3.3. Dynamic contact angle

Following Hoffman's relation, the dynamic contact angle Θ depends on the capillary number $\mathrm{Ca} = \mu V_{cl}/\sigma$, where V_{cl} is the propagation velocity of the contact line. Several empirical dependences of Θ on Ca exist in the literature. In the present work we use the formula in [24]

$$\Theta(\mathrm{Ca}, \Theta_0) = f_{Hoff}[\mathrm{Ca}a + f_{Hoff}^{-1}(\Theta_0)] \tag{8}$$

where $f_{Hoff}^{-1}(\Theta)$ is the inverse function of the function $f_{Hoff}(\mathrm{Ca})$ which is defined as

$$f_{Hoff}(\mathrm{Ca}) = \arccos\left\{1-2\tanh\left[5.16\left(\frac{\mathrm{Ca}}{1+1.31\,\mathrm{Ca}^{0.99}}\right)^{0.706}\right]\right\} \tag{9}$$

and Θ_0 is the static contact angle.

Recent investigations and also the dynamic contact angles measured in this study indicate that such correlations are of very limited validity throughout the entire spreading and receding process, in which case Θ_0 becomes only a fitting parameter. It is important to note that the Reynolds number associated with drop impact is much larger than 1. During the spreading phase the inertial effects cannot be neglected even in the region near the contact line of the characteristic length corresponding to one pixel of the high-speed camera. Therefore, Hoffman's relation based on the steady creeping flow approximation (as above) is not valid during the rapid spreading of the low-viscous drop. The discrepancy between Hoffman's relation and the experimental data of the dynamic contact angle during the spreading was shown in [13]. This angle is nearly 180° at the very initial stage of the impact, and reaches some nearly constant value of about 120°. During this period of the spreading, the spread factor does not depend on the surface wettability [6].

4. Results and discussion

4.1. Uniform surface

Some very typical results of normal drop impacts onto a surface of uniform wettability for three different Reynolds numbers are shown in figure 5. The silicon wafer is coated with polystyrene,

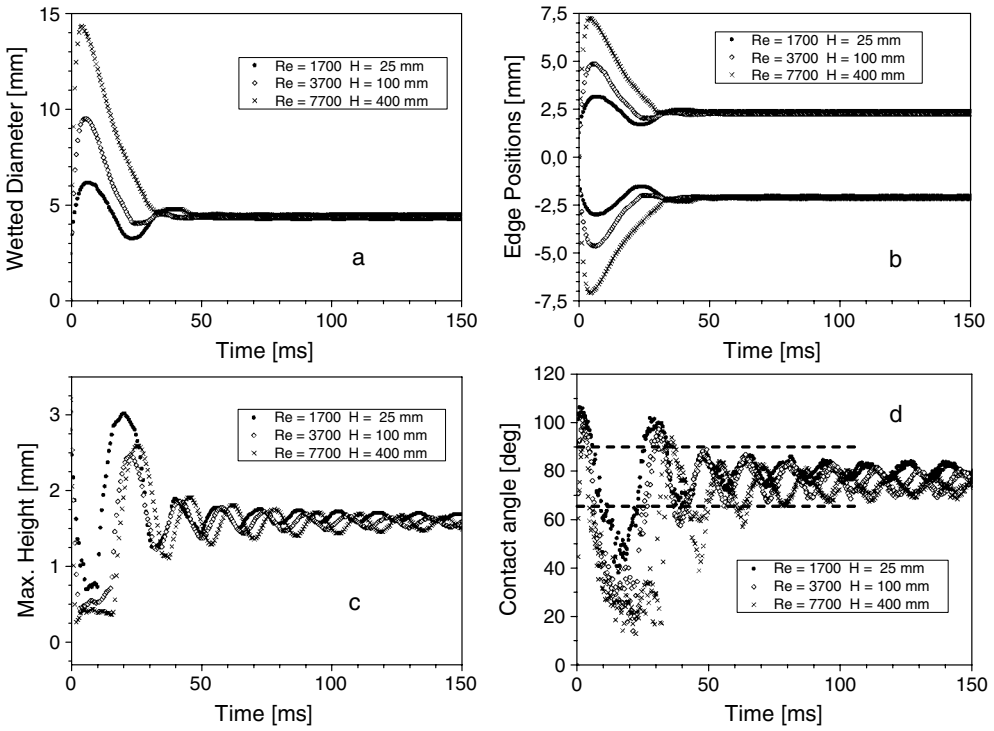

Figure 5. Normal drop impact onto surface I without a wettable spot, $D_0 = 3.2 \pm 0.1$ mm. (a) Wetted diameter, (b) edge positions of the drop, (c) apex height, (d) contact angle.

exhibiting advancing and receding contact angles of 90° and 65° respectively (surface I). A drop of diameter 3.2 ± 0.1 mm was released from heights of 25, 100 and 400 mm, yielding impact velocities of 0.52, 1.17 and 2.51 m s^{-1} respectively.

The drop diameter and edge positions are given in dimensional form as a function of time in figures 5(a) and (b). Clearly the maximum spread diameter achieved depends on the impact velocity, although the time to achieve this maximum appears to be almost constant. Hence, in terms of dimensionless time, $t^* = tU_0/D_0$, the time of maximum spread scales roughly with impact velocity. The symmetry of the normal impact is confirmed in figure 5(b).

According to [6] the final wetted diameter will lie between the diameters

$$\frac{d_\mathrm{r}}{D_0} = 2\left[\frac{\sin^3\Theta_\mathrm{rec}}{2(1-\cos\Theta_\mathrm{rec})(2-\cos\Theta_\mathrm{rec}-\cos^2\Theta_\mathrm{rec})}\right]^{1/3}$$
$$\frac{d_\mathrm{a}}{D_0} = 2\left[\frac{\sin^3\Theta_\mathrm{adv}}{2(1-\cos\Theta_\mathrm{adv})(2-\cos\Theta_\mathrm{adv}-\cos^2\Theta_\mathrm{adv})}\right]^{1/3} \tag{10}$$

given for the advancing and receding contact angle respectively. These diameters are based on a truncated spherical cap model of the final metastable state of the drop. For the conditions shown in figure 5 these diameters take the values $d_\mathrm{a} = 4.03$ mm and $d_\mathrm{r} = 4.94$ mm, values which indeed straddle the final measured drop diameter of 4.3–4.6 mm. Note that in the receding phase, the drop overshoots its final diameter, exhibiting oscillation behaviour, more pronounced for the case of the lowest Reynolds number.

Although the drop contact line is stationary after approximately 50 ms, the drop is still oscillating, as seen by the apex height variations and contact angle variations in time, shown

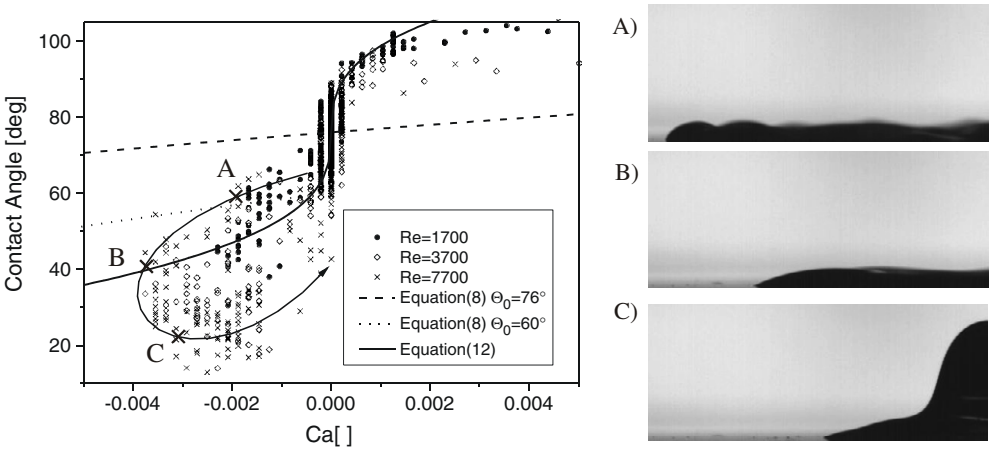

Figure 6. Drop impact on a homogeneous region of surface I, $D_0 = 3.2 \pm 0.1$ mm. Contact angle versus capillary number with three images of different receding stages for $Re = 7700$.

in figures 5(c) and (d). The frequency of oscillation is approximately the same for all impact Reynolds numbers, as expected for a constant volume of liquid. A small (almost constant) phase shift between the different cases indicates different damping forces acting on the drop during the initial impact stage, probably attributable to the nonlinear viscous forces on the wall.

The contact line movement ceases once the contact angle oscillations fall within the band of 65°–90°, i.e. at approximately 50 ms for all cases (see figure 5(d)). During this period of oscillation the damping is indeed very small—the viscous forces on the wall are comparatively small.

From the data as shown in figure 5 it is possible to plot the measured contact angle as a function of capillary number, given by $\mathrm{Ca} = \mu V_{\mathrm{cl}}/\sigma$, where V_{cl} is the measured velocity of the contact line: positive in the advancing stage and negative in the receding phase. Such a graph is shown in figure 6. For reference, the correlation given in (8) has been added to this graph using $\Theta_0 = 60°$ and 76°. The former value is shown because it is used later in the analytic computations. The latter value is the asymptotic value of the measured contact angle 0.4 s after impact (not shown here).

The measurements exhibit a very strong scatter, more so for receding than for advancing conditions. This is a very clear demonstration that the hydrodynamics within the drop are very influential on the dynamic contact angle and that simple correlations as given above can only be approximations of the actual physical situation.

A further arrowed curve has been added to the diagram in figure 6, showing an approximate time evolution of the scattered values for a receding contact line. The images for three typical drop states are also given in the figure to underline the wide variety of hydrodynamic conditions which can be encountered for any given contact line velocity.

A third correlation is shown in figure 6, which has been prompted by the suggestion in [24] of the function

$$\Theta(\mathrm{Ca}) = 4.54\,\mathrm{Ca}^{0.353}. \tag{11}$$

The final correlation is given by

$$\Theta(\mathrm{Ca}) = \Theta_0 + \mathrm{sgn}(\mathrm{Ca})\,4.54|\mathrm{Ca}|^{0.353} \tag{12}$$

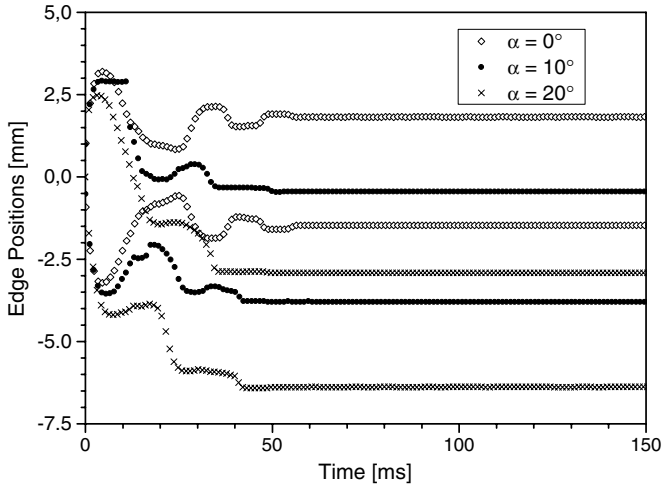

Figure 7. Inclined drop impact onto the homogeneous region of surface II, $D_0 = 2.5 \pm 0.1$ mm, $Re = 2200$. Edge positions of the drop.

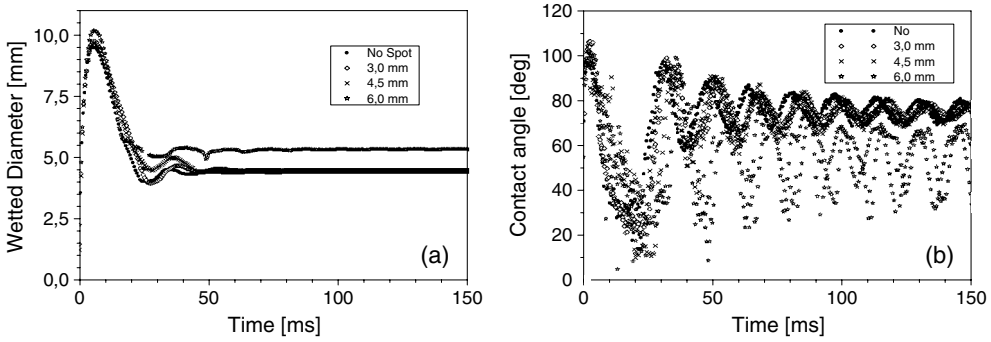

Figure 8. Influence of the spot size on normal impact on surface I, $D_0 = 3.2 \pm 0.1$ mm, $Re = 3700$. Temporal evolution of (a) the wetted diameter and (b) the dynamic contact angle.

whereby $\Theta_0 = 76°$. While this improves the agreement to the measured data, large scatter remains in the receding phase.

Finally, the influence of inclination angle on drop impacts onto a homogeneous surface is shown in figure 7. Although the drop comes to rest even at the highest inclination of $\alpha = 20°$, the spreading and drop dynamics are clearly influenced by gravity. Not only does the resting position of the drop shift with inclination angle, but also the final wetted length of the surface increases slightly; 0°: 3.3 mm, 10°: 3.35 mm, 20°: 3.46 mm. As before, the contact line ceases to move after about 50 ms, somewhat earlier for the top edge (receding) compared with the bottom edge (advancing).

4.2. Impact onto chemically structured surfaces

Experiments with various sizes of wettable spots on the impact surface demonstrate the influence the spot can have on the final drop size, at least for the case of normal impact at the centre of the spot. Such a result is shown in figure 8 for spot sizes of 3.0, 4.5 and 6.0 mm

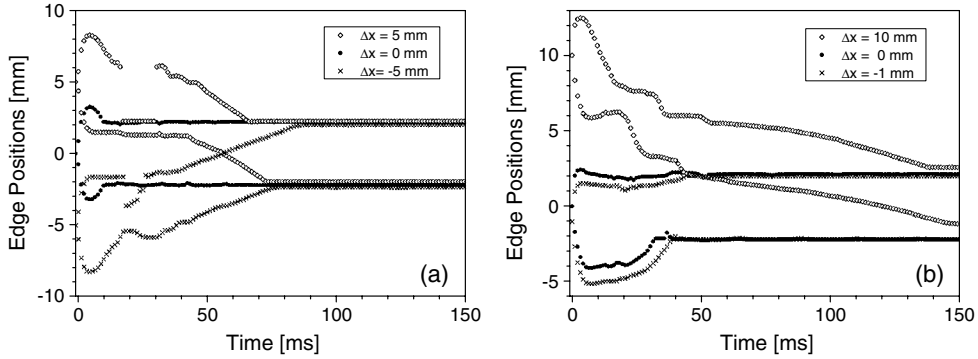

Figure 9. Drop edge position for impact points displaced from the centre of the wettable spot: surface II, spot diameter 4.5 mm, $D_0 = 2.5 \pm 0.1$ mm, $Re = 2200$. (a) Normal impact, (b) inclined impact with the impact angle $\alpha = 20°$.

in diameter and for an impact Reynolds number of 3700 ($D_0 = 3.2$ mm). The diameters given by (10) for the non-wettable surface surrounding the spot were $d_a = 4.03$ mm ($\Theta_{adv} = 93°$) and $d_r = 4.94$ mm ($\Theta_{rec} = 65°$). Within the spot ($\Theta_{spot} = 54°$), the diameter was $d = 5.4$ mm. Thus, only for the largest spot does the surface structure influence the spreading significantly. A small change in spreading velocity can be detected as the drop recedes across the border of the largest spot. Also, the contact angle oscillations are much larger when the drop is positioned within the wettable spot and they are centred about the lower contact angle of $\Theta_{spot} = 54°$.

In the initial spreading phase the contact line advances across the change in contact angle for all cases shown in figure 8; however, here no change in spread velocity is detectable, confirming the fact that this stage is completely dominated by inertial effects and that it remains uninfluenced by contact angle. Figure 8(b) also confirms that throughout the expansion phase, which extends up to about 7 ms, the contact line movement is the same for all cases; deviations become apparent only once the receding phase begins.

The potential for self-centring of the drop was first examined by moving the point of impact away from the centre of the wettable spot. Results from such an experiment are shown in figure 9 for normal and inclined ($\alpha = 20°$) impacts. In all cases a drop of $D_0 = 2.5$ mm diameter and an impact velocity of $U_0 = 0.91$ m s^{-1} ($Re = 2200$) were used. The wettable spot size was 4.5 mm and the contact angles outside the spot were $\Theta_{adv} = 93°$, $\Theta_{rec} = 86°$. In this case the equilibrium diameter of the drop using the contact angle of the wettable spot ($\Theta_{spot} < 20°$) corresponded to $d_{spot} > 6.2$ mm; hence the drop is expected to fit within the wettable spot.

The results in figure 9 indicate that for all shown displacements, a self-centring effect was achieved. For normal impacts this was true for impact displacements up to 5 mm. For a displacement of 6 mm the contact line of the drop never reached the wettable spot and self-centring was therefore impossible.

Self-centring on inclined surfaces is demonstrated in figure 9(b), in which impact points above the centre of the wettable spot are shown as positive displacements. Obviously, due to gravity, much larger positive displacements can be tolerated than negative ones, to still achieve self-centring. In fact, self-centring for positive displacements will always occur if the lower contact line reaches the wettable spot. This is just fulfilled for the displacement $\Delta x = 10$ mm shown in figure 9, which can be realized by comparing to the same case without a wettable spot shown in figure 7 ($\alpha = 20°$).

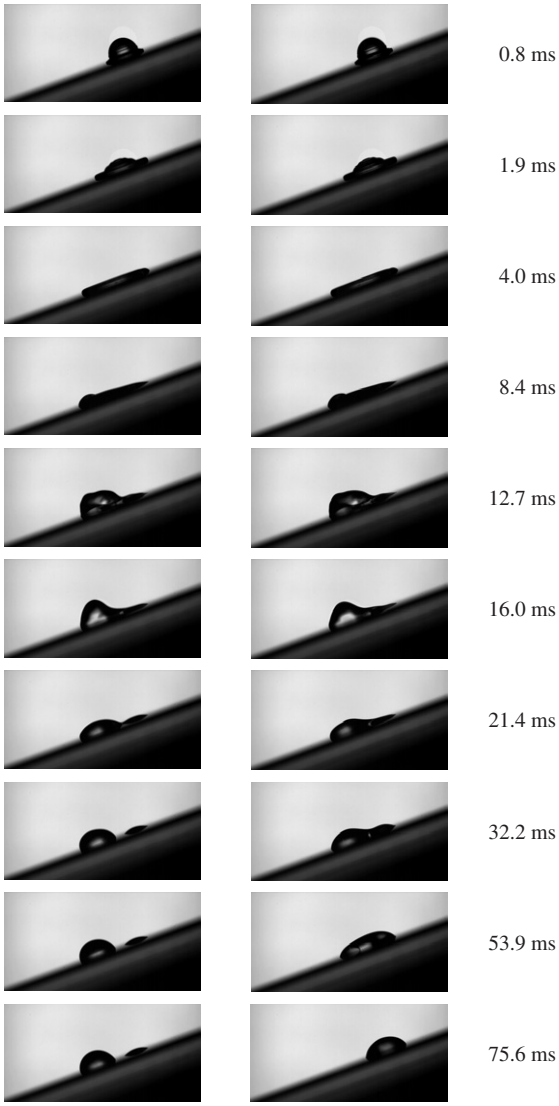

Figure 10. Two sequences of inclined drop impact ($\alpha = 20°$): surface II, spot diameter 4.5 mm, $D_0 = 2.5 \pm 0.1$ mm, $Re = 2200$.

For negative displacements this rule, derived for the upper contact line, does not hold strictly true, since the gravitational force must be overcome, which requires a certain minimum overlap of the spreading drop and the wettable spot. This is illustrated in figure 10, in which a sequence of pictures is shown for two repetitions of the same experiments: a 2.5 mm drop impacts with a displacement of 2 mm onto an inclined surface ($\alpha = 20°$) with a 4.5 mm wettable spot. In the first sequence the drop disjoins and only a portion remains on the wettable spot. In the second sequence the entire drop is successfully self-centred. For these conditions the first sequence is representative of about 70% of the experiments—apparently this is very close to a limiting condition.

Further experiments are presently underway to more systematically quantify the conditions for self-centring. A first result is shown in figure 11 for an impact Reynolds number of 2200

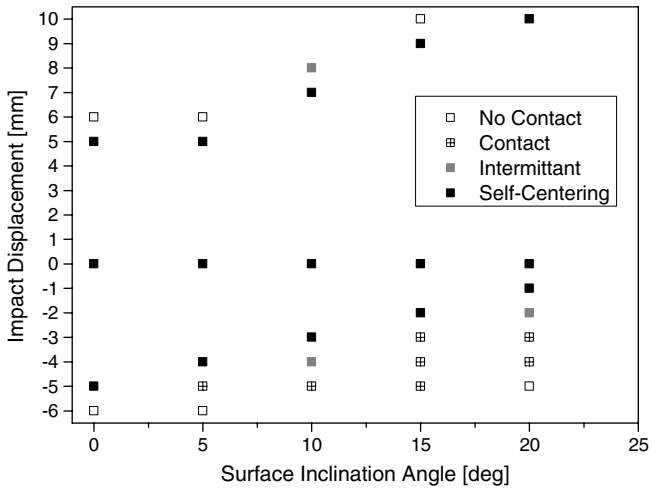

Figure 11. Summary of self-centring conditions: surface II, spot diameter 4.5 mm, $D_0 = 2.5 \pm 0.1$ mm, $Re = 2200$.

and for various tilt angles. In this diagram four possible outcomes of the drop impact have been distinguished: no contact, contact, intermittent, and self-centring. No contact refers to conditions under which the spreading drop makes no contact with the wettable spot. Contact signifies liquid contact with the wettable spot but no self-centring. Intermittent means self-centring is sometimes observed but not always (e.g. figure 10) and self-centring indicates that self-centring is always observed for those particular impact conditions. This classification is found useful, since the experiments are performed only in discrete steps of inclination angle and impact displacement.

The results presented in figure 11 indicate that the delineation between the self-centring and not self-centring is very abrupt for positive displacements and for all inclination angles. However, for negative displacement, as the inclination angle increases, the necessary liquid overlap on the wettable spot for self-centring increases considerably—an obvious consequence of the increased gravitational force.

4.3. Comparison of theory with experiment

The theoretical model developed in [22] and yielding the rim radius given by (2) is for a surface of uniform wettability, and, as the comparison shown in figure 12 indicates, agreement with experiment is rather good for normal impacts. In order to present the data obtained for different impact parameters in the most generalized form, the results are given in the dimensionless form.

For impact onto chemically structured surfaces the spreading is no longer axisymmetric and the wetted spot is no longer circular. Nevertheless, the two-dimensional assumptions of the model will still be considered valid and the advancement of the two drop edges (L: left; R: right) in the symmetry plane will be considered. The dynamic contact angle during the receding phase is determined using the expression (8) using the local receding contact angle of $\Theta_{\mathrm{rec}}(\mathrm{Ca})$.

As discussed briefly in section 3, the hydrodynamics near the contact line influences the dynamic contact angle such that equation (8) must be adjusted. Also in [24] the static contact angle Θ_{static} has not been used as Θ_0, but some other empirically more appropriate value. In the results presented below a value of $\Theta_{\mathrm{rec,static}} = 60^\circ$ is used for the outer hydrophobic regions of the substrate, and $\Theta_{\mathrm{rec,static}} = 40^\circ$ for the spot region.

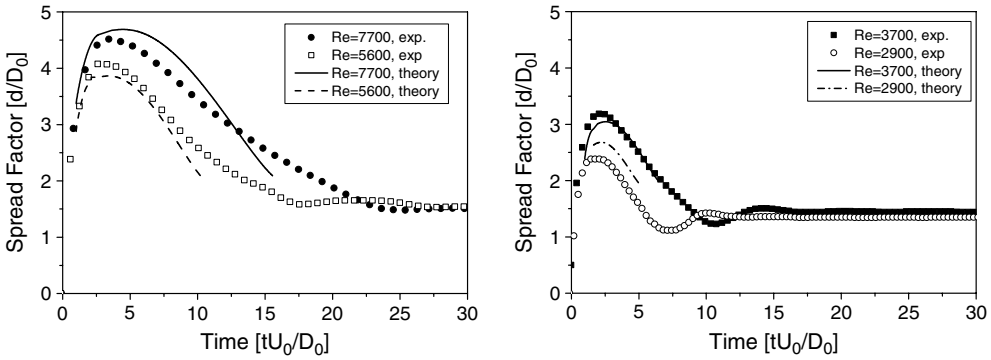

Figure 12. Drop impact onto surface I. Comparison of experimental data to results of the theoretical model. The receding static contact angle is $\Theta_{\mathrm{rec,static}} = 60°$, and the drop diameter is $D_0 = 3.2$ mm.

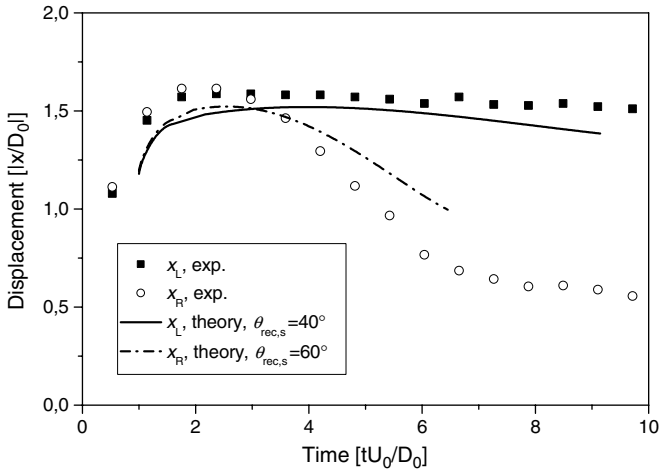

Figure 13. Drop impact on surface I, spot diameter 6 mm. Comparison of experimental data for the distance to the left ($\bar{x}_{\mathrm{L}}$) and right ($\bar{x}_{\mathrm{R}}$) edge of the wetted spot. The receding static contact angles are $\theta_{\mathrm{rec,static}} = 60°$ at the right edge, and $\Theta_{\mathrm{rec,static}} = 40°$ at the left edge of the drop. The impact parameters are: $Re = 3700$, $We = 59$.

In figure 13 the theoretical predictions and the experimental data for the dimensionless positions of the drop edges are compared for a drop impact onto a 6 mm wettable spot (surface I) such that the left edge spreads on the wettable spot ($\Theta_{\mathrm{rec,static}} = 40°$), whereas the right edge spreads on the hydrophobic substrate ($\Theta_{\mathrm{rec,static}} = 60°$). The contact line recedes on the hydrophobic surface and does not recede on the wettable spot. The agreement between theory and experiment is very good.

Now the case of a contact line crossing a boundary of contact angle variation is considered. The boundary B separates two regions on the substrate, S_1 and S_2, with different contact angles, Θ_1 and Θ_2. Four cases can be distinguished corresponding to advancing or receding contact lines or whether $\Theta_1 > \Theta_2$ or $\Theta_1 < \Theta_2$. These cases are schematically illustrated in figure 14. The advancing cases are not relevant in this particular study, since the advancing stage after impact is inertia dominated. Therefore the more interesting situation is the receding case when $\Theta_1 > \Theta_2$; that is, the drop is receding onto the wettable spot (figure 14(c)).

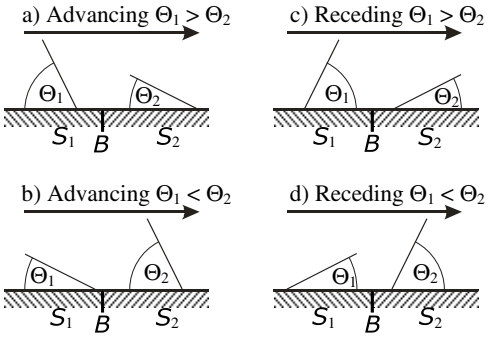

Figure 14. Schematic illustration of possible contact line crossing of a contact angle boundary.

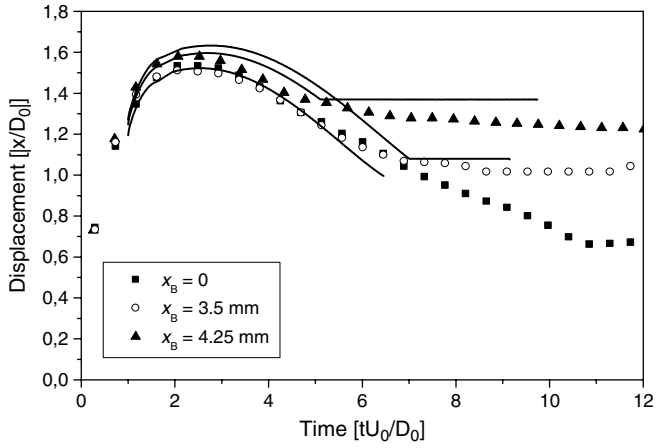

Figure 15. Drop impact on surface I, spot diameter 6 mm. Data for the dimensionless drop edge, $\bar{x}$, as a function of dimensionless time for different positions $\bar{x}_B$ of the boundary B. The contact angle jumps at B from $\Theta_{\text{rec,static}} = 60°$ to 40°. The impact parameters are: $Re = 3500$, $We = 55$ at $x_B = 0$; $Re = 4210$, $We = 75$ at $x_B = 3.5$ mm; $Re = 4000$, $We = 70$ at $x_B = 4.25$ mm.

As the contact line moves to the boundary B, it stays there until the dynamic contact angle decreases to Θ_1, after which it continues onto the more wettable region.

This situation has been studied experimentally and then theoretically computed, using, as above, $\Theta_{\text{rec,static}} = 60°$ and $\Theta_{\text{rec,static}} = 40°$ as Θ_0 in (8). The results of this comparison are shown in figure 15 for normal impact onto a 6 mm spot with three impact point displacements, $x_B = 0$, 3.5 and 4.25 mm. The exact impact parameters are given in the figure caption. The theory successfully predicts the observed contact line positioning for the two displaced impacts, which confirms the suitable choices of $\Theta_{\text{rec,static}}$.

5. Conclusions

The impact of drops onto chemically structured surfaces has been experimentally and theoretically investigated. The structures consisted of wettable spots of various diameters on otherwise hydrophobic surfaces, characterized by the advancing and receding contact angles.

The results of this study demonstrate the possibility of, and the conditions under which, self-centring of a liquid drop can occur, also for the case of inclined surfaces.

A theoretical model for the temporal evolution of the drop edges during the advancing and receding phase has been formulated. This model accounts for internal effects, capillary and viscous forces, and the dynamic contact angle. The mass and the momentum balance equation of the rim formed at the edges of the drop by the surface tension are considered. The theory is based on the assumption that the motion of the rim can be determined by the local conditions only, in particular by the instantaneous local contact angle. An empirical correlation has been used to describe the dynamic contact angle, and the good agreement between experiment and theory validates this choice.

Acknowledgments

We acknowledge the Deutsche Forschungsgemeinschaft (DFG) for the financial support within the priority program 'Wetting and Structure Formation at Interfaces', grants Ru 489/11 and Tr 194/12.

References

[1] Worthington A M 1877 *Proc. R. Soc.* **25** 261
[2] Rein M 1993 *Fluid Dyn. Res.* **12** 61
[3] Rioboo R, Tropea C and Marengo M 2001 *At. Sprays* **11** 155
[4] Maier C, aus der Wiesche S and Hofer E P 2000 *Tech. Proc. 2000 Int. Conf. Modelling and Simulation of Microsystems (San Diego, CA, 27–29 March 2000)* p 586
[5] Huber L, McCartney H A and Fitt B D L 1997 *Agric. Forest Meteorol.* **87** 201
[6] Rioboo R, Marengo M and Tropea C 2002 *Exp. Fluids* **33** 112
[7] Chandra S and Avedisian C T 1991 *Proc. R. Soc.* A **432** 13
[8] Fukai J, Shiiba Y, Yamamoto T, Miyatake O, Poulikakos D, Megaridis C M and Zhao Z 1995 *Phys. Fluids* **7** 236
[9] Mao T, Kuhn D C S and Tran H 1997 *AIChE J.* **43** 2169
[10] Pasandideh-Fard M, Qiao Y M, Chandra S and Mostaghimi J 1996 *Phys. Fluids* **8** 650
[11] Stow C D and Hadfield M G 1981 *Proc. R. Soc.* A **373** 419
[12] Range K and Feuillebois F 1998 *J. Colloid Interface Sci.* **203** 16
[13] Šikalo Š 2002 *Dr.-Ing. Dissertation* TU Darmstadt, Darmstadt, Germany
[14] Bergeron V 2003 *C. R. Physique* **4** 211
[15] Prunet-Foch B, Legay F, Vignes-Adler M and Delmotte C 1998 *J. Colloid Interface Sci.* **199** 151
[16] Fukai J, Zhao Z, Poulikakos D, Megaridis C M and Miyatake O 1993 *Phys. Fluids* **5** 2588
[17] Bussmann M, Chandra S and Mostaghimi J 2000 *Phys. Fluids* **12** 3121
[18] Geldorp W I, Rioboo R, Jakirlic S, Muzaferija S and Tropea C 2000 *Proc. 8th Int. Conf. On Liquid Atom. and Spray Systems (Pasadena, CA, July 2000)*
[19] Renardy Y, Popinet L, Duchemin L, Renardy M, Zaleski S, Josserand C, Drumright-Clarke M A, Richard D, Clanet C and Quere D 2003 *J. Fluid Mech.* **484** 69
[20] Prucker O, Naumann C, Rühe J, Frank C and Knoll W 1999 *J. Am. Chem. Soc.* **121** 8766
[21] Prucker O, Habicht J, Park I J and Rühe J 1999 *Mater. Sci. Eng.* C **8/9** 291
[22] Roisman I V, Rioboo R and Tropea C 2002 *Proc. R. Soc.* A **458** 1411
[23] Yarin A L and Weiss D A 1995 *J. Fluid Mech.* **283** 141
[24] Kistler S F 1993 *Wettability* (*Surfactant Science* vol 49) ed J C Berg (New York: Dekker) pp 311–429